Imaging dislocations in gallium nitride across broad areas using atomic force microscopy

S. E. Bennett, D. Holec,[a] M. J. Kappers, C. J. Humphreys, and R. A. Oliver[b]
Department of Materials Science and Metallurgy, University of Cambridge, Pembroke Street, Cambridge CB2 3QZ, United Kingdom

(Received 31 March 2010; accepted 26 April 2010; published online 4 June 2010)

We have employed an atomic force microscope with a high sampling rate to image GaN samples grown using an epitaxial layer overgrowth technique and treated with silane and ammonia to enlarge the surface pits associated with threading dislocations (TDs). This allows TDs to be identified in high pixel density images tens of microns in size providing detailed information about the spatial distribution of the TDs. An automated software tool has been developed, which identifies the coordinates of the TDs in the image. Additionally, we have imaged the same sample using Kelvin probe force microscopy, again at high pixel density, providing data about the local changes in surface potential associated with hundreds of dislocations. © *2010 American Institute of Physics.*
[doi:10.1063/1.3430539]

I. INTRODUCTION

While electronic and optoelectronic devices based on the heteroepitaxial growth of GaN have achieved significant success, an imperative remains to reduce the density of defects in these materials. High densities of threading dislocations (TDs) have been shown to increase leakage currents in blue and green light-emitting diodes (LEDs),[1] shorten the lifetime of laser diodes,[2] reduce the efficiency of LEDs emitting in the near ultraviolet,[3] and lower electron mobilities in high electron mobility transistors.[4]

In order to assess the effectiveness of TD density reduction strategies, accurate methods for the assessment of TD densities are required and a number of TD imaging techniques have been explored. Transmission electron microscopy (TEM) images taken in plan view can provide insight into both TD densities and the TD types present in a sample, and a multibeam imaging technique has been developed, which reveals with high contrast all the screw, edge, and mixed TDs in a single plan-view image over an approximately 5×5 μm^2 area even when the specimen is bent.[5] However, TEM specimen preparation is time consuming and imaging over areas larger than those described in Ref. 5 remains difficult. Cathodoluminescence (CL) in the scanning electron microscope provides an alternative route[6] to the assessment of dislocation densities across large areas in films with relatively low TD densities, since TDs appear to act as nonradiative recombination centers, giving rise to dark spots in CL images. However, in films with higher TD densities or with regions of locally high TD density, it may be impossible to separate the dark spots arising from closely spaced TDs, reducing the accuracy of this approach. Also, a method for distinguishing between different TD types in CL images has yet to be established. X-ray microbeam analysis can also give an insight into the spatial arrangement of dislocations across broad areas[7] but has limited spatial resolution compared to most imaging techniques (beam sizes of about 0.5 μm are typical[7]) and requires the use of a synchrotron x-ray source, which is not readily available to most researchers.

Quantification of TD densities in atomic force microscopy (AFM) relies on the fact that the termination of TDs at an epilayer surface gives rise to a small pit, a topographic change which can be imaged in AFM. However, for as-grown GaN epilayers, the pits relating to edge-type TDs are extremely small and success in imaging these pits is highly dependent on the tip used. A number of different techniques exist to increase the size of these pits.[8–11] Here, we will exploit a technique which we have previously developed for use with samples grown by metal-organic vapor phase epitaxy (MOVPE): an *in situ* treatment using silane and ammonia, which may be performed immediately after growth in the MOVPE reactor and which enlarges the size of the pits, allowing straightforward imaging.[12] The treatment results in pits relating to edge-type TDs having a width of around 35 nm and pits relating to screw-or mixed-type TDs having a larger width of around 55 nm. Hence, the pits remain small enough that it is possible to distinguish adjacent dislocations in most samples, and the pit size may be used to distinguish edge-type TDs from those with a screw component. Comparison of AFM and TEM data from the same sample suggests that the size of the pits can reliably be used to estimate the proportion of edge-type dislocations in GaN.[12]

Our AFM-based technique for determination of TD densities has successfully been applied to a range of samples with fairly uniformly distributed TDs and with TD densities from about 6×10^7 cm^{-2} (Ref. 13) to 5×10^9 cm^{-2}.[14] This AFM-based method has so far mostly been applied to *c*-plane GaN. However, the same method has recently been used to assess dislocation densities in nonpolar *a*-plane GaN

[a]Present address: Department of Physical Metallurgy and Materials Testing, University of Leoben, A-8700 Leoben, Austria.
[b]Author to whom correspondence should be addressed. Electronic mail: rao28@cam.ac.uk.

films.[15] In these films, it has been observed that for dislocation densities up to about 6×10^9 cm^{-2}, the dislocation densities estimated by AFM and those estimated by TEM are very similar. However, for samples with dislocation densities of above 10^{10} cm^{-2}, the AFM-based method underestimates the dislocation density.[15]

Typically, multiple 3×3 or 5×5 μm^2 images containing 512×512 pixels are taken at random locations, allowing for an effective sampling of the TD density across the wafer. However, as ever-lower TD densities are achieved, the number of TD pits found in such an image decreases, so that in order to reduce the statistical errors in calculating the mean TD density, large numbers of images must be recorded. Additionally, for some TD density reduction techniques—such as epitaxial layer overgrowth (ELOG)—the distribution of TD pits across the surface is very nonuniform, and small images taken at random positions do not give useful information about this distribution. Hence, the need arises to image TDs across much larger areas. ELOG typically gives rise to material with alternating bands of low and high TD densities with a periodicity of several microns so that images tens of microns in size in which the TD pits can be resolved are desirable.

As an example, consider a 30×30 μm^2 image. Clearly, to achieve the same pixel density as is found in a typical 512×512 pixel, 3×3 μm^2 image, 5120×5120 pixels are required. Data sets containing such large numbers of pixels cannot be collected on many typical AFM systems since achieving a high number of pixels per line is not simply a question of the software issues involved in handling large amounts of data. When an AFM data set is taken, the height of the surface is sampled many times for each pixel, and the data recorded are an average of these samples, giving a reasonably low noise image. For a fixed scan rate (i.e., a fixed time taken to scan one line) and a fixed sampling rate, increasing the number of pixels per line must reduce the number of times the surface height is sampled for each pixel, increasing the noise level in the image. Hence, in order to achieve good quality images with very large numbers of pixels, the sampling rate used in AFM must be increased. Here, we describe the use of a Veeco Nanoscope V controller, which uses a sampling rate of 500 kHz (a significant improvement on its predecessor, the Nanoscope IV, which used a sampling rate of 64 kHz), to image ELOG GaN across broad areas with a high pixel density. We also demonstrate the combination of broad area, high pixel density topographic imaging with imaging of local surface potential, and describe methods for the automated analysis of both the topographic and the surface potential data.

II. METHODS

An ELOG GaN sample was grown on a *c*-plane sapphire substrate miscut $0.25°\pm0.10°$ toward $(11\bar{2}0)$ using a 6×2 in. Thomas Swan close-coupled showerhead MOVPE reactor. Trimethylgallium, silane (SiH_4), and ammonia (NH_3) were used as precursors. Hydrogen (H_2) was the carrier gas. Initially a 500 nm thick GaN seed layer was deposited by first growing an ~30 nm nucleation layer at 540 °C and thereafter growing a two-dimensional GaN layer at a temperature of 1005 °C and a V:III ratio of ~1310. Next, a SiN_x mask was deposited *in situ* for 1 h at 860 °C. The mask was patterned *ex situ* using optical lithography to form 5 μm stripes and 5 μm windows parallel to the *m* direction ($[1\bar{1}00]$ direction). A two-step ELOG process[16] was then applied: initial GaN regrowth through the windows occurred at 980 °C, 400 Torr, and a V:III ratio of 200 to form stripes of material with a triangular cross section bounded by $\{11\bar{2}2\}$ facets. In the second step, the temperature was then increased to 1020 °C, the pressure decreased to 100 Torr, and the V:III ratio increased to 1300 to favor lateral growth, so that the stripes coalesced to form a planar GaN epilayer. In order to increase the size of the TD pits, the sample surface was then exposed to a SiH_4 flux of 200 nmol/min under a 20 slm NH_3/H_2 flow ($NH_3:H_2=1:1$) at 860 °C for 240 s.[12]

AFM was carried out in intermittent contact mode using a Veeco Dimension 3100 microscope equipped with a Nanoscope V controller. Veeco RTESP tips with a nominal apex radius of 8 nm were used when only topographic images were required, while when topographic imaging was combined with Kelvin probe force microscopy (KPFM), Veeco SCM-PIT tips were employed, which are coated with 20 nm of Pt/Ir and have a nominal apex radius of 20 nm.

For topographic imaging, scan sizes of 30 μm $\times30$ μm were employed with 4992×4992 pixels. Due to the use of miscut substrates, atomic steps on the samples run roughly parallel to $[11\bar{2}0]$ whereas the ELOG mask stripes run in a perpendicular direction along $[1\bar{1}00]$. The sample was aligned so that the fast scan direction for imaging was roughly halfway between these two key directions. Image optimization was initially carried out for 3×3 μm^2, 512×512 pixel images, and the scan size was then gradually increased, while the scan rate was decreased and the pixel density was kept roughly constant. In order to take high quality 30×30 μm^2 images, low scan rates (around 0.3 Hz) were typically used, resulting in imaging times in excess of 5 h. Both topographic and amplitude error data were recorded.

TEM data were used to aid in interpretation of the AFM data. The sample was examined using a Philips CM30 300 kV analytical TEM with a LaB_6 source. Weak-beam dark field (WBDF) images were taken using a g-$3g$ diffraction condition.

For KPFM imaging (also referred to as surface potential microscopy), slightly lower scan sizes and pixel densities and slightly higher scan rates were used than for the basic topographic measurements. A brief description of the KPFM technique will illustrate why this was necessary: in KPFM, the tip initially scans the surface in tapping mode and the variations in surface height are recorded. Then, the tip is scanned over the same region of the sample a second time but is lifted a small distance away from the sample and then follows the topographic contour recorded on the previous scan line. (This second scan over the same region is known as a lift scan line.) During the lift scan line, instead of using a piezoelement to cause cantilever oscillation, an oscillating voltage of magnitude V_{ac} is applied to the tip, which gives rise to an oscillating force

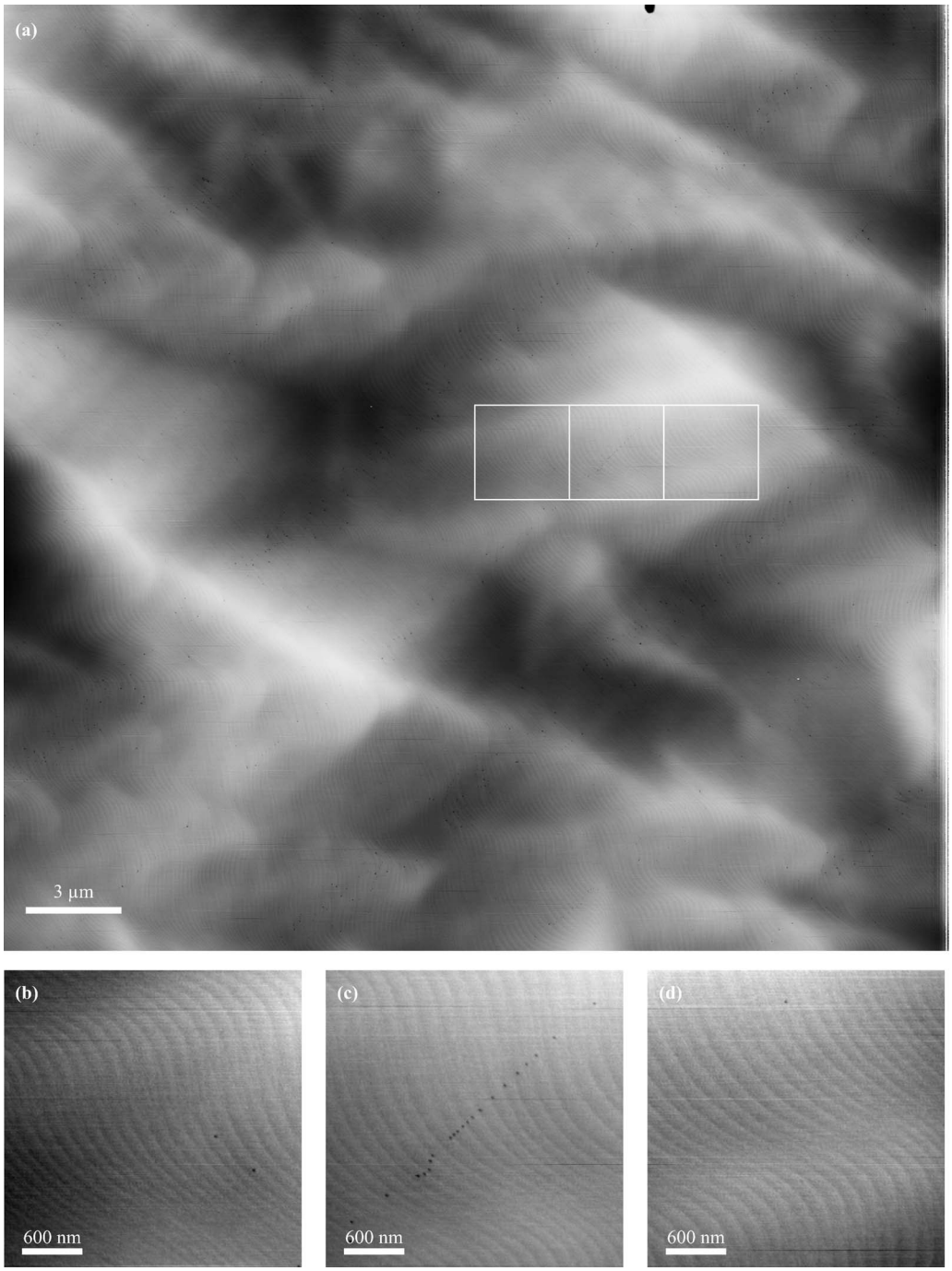

FIG. 1. (a) A typical broad area topographic AFM image of ELOG GaN: $30\times30\ \mu m^2$ image from a data set containing 4992×4992 pixels. Image z scale $(z)=40$ nm. The detail from the original image may not be visible in print copies, so an electronic version of the original image is provided as online supplementary material (Ref. 18). (b)–(d) Portions of the image in (a) shown at a larger size to allow the details to be more easily observed. $z=7$ nm. These images relate to the sections of (a) indicated by white boxes, with (b) corresponding to the left-hand box, (c) to the middle box, and (d) to the right-hand box.

$$F=\frac{dC}{dz}\Delta V_{dc}V_{ac}, \tag{1}$$

where dC/dz is the tip-sample capacitance gradient and ΔV_{dc} is the difference in potential between the tip and sample. If the potential on the tip is adjusted so that it matches the potential on the sample, ΔV_{dc} is zero, and the cantilever experiences no oscillating force. Hence, by using a feedback circuit to adjust the tip potential to achieve zero cantilever oscillation, a quantitative map of the sample surface potential may be recorded.[17] However, because of the necessity of recording the surface potential data during a separate scan line to the topographic data, KPFM scans take twice as long to complete as data sets in which only topographic data are recorded, for the same tip speed. Hence, in order to reduce the amount of time taken to record the KPFM data, the scan size and the number of pixels were reduced in comparison to the data sets for which only topography was recorded. The topographic and KPFM data were analyzed using bespoke automated routines which will be discussed in more detail in Sec. IV.

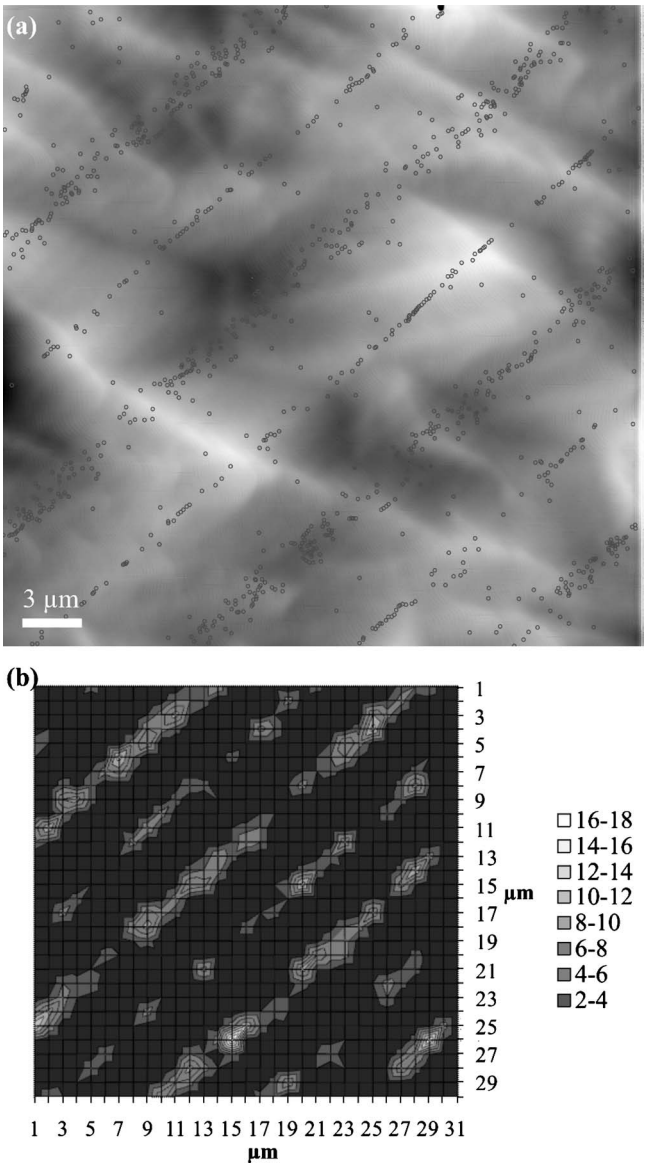

FIG. 2. (a) Topographic AFM image from Fig. 1(a) with gray circles added to indicate the positions of the TD pits. (b) TD density map created by dividing Fig. 1(a) into 1×1 μm^2 square boxes and counting the number of TDs in each box. The resulting data matrix was then plotted in MICROSOFT EXCEL as a contour plot. The key is in units of TDs/μm^2.

III. RESULTS AND DISCUSSION

Figure 1(a) shows a typical 30×30 μm^2 AFM image recorded at 4992×4992 pixels. Since in a print copy of this image the level of detail recorded in the original data set is not preserved, an electronic copy of the full high resolution image is also provided as supplementary online material.[18] Additionally, Figs. 1(b)–1(d) show small portions of the image from the areas marked by white boxes in Fig. 1(a). In these images, terraces and steps can clearly be seen and measurement of the step heights reveals that these are comprised of a mixture of single monolayer (~0.25 nm) and bilayer (~0.5 nm) steps. Small pits relating to TDs are also observed, which are 5–10 pixels in width in the original data set.

Figure 2 illustrates more effectively the information which the large area, high pixel density scan provides about the distribution of TDs in the ELOG material. In Fig. 2(a), the data in Fig. 1(a) are displayed with the dislocation pits ringed in gray. The rings were applied to this image manually but we are now also able to perform the same operation using an automated routine, which will be described in Sec. IV. Figure 2(b) is a TD density map in which the image has been divided up into 1×1 μm^2 square boxes and the number of TDs in each box has been recorded and the resulting data matrix plotted in MICROSOFT EXCEL as a contour plot. Both parts of Fig. 2 show bands of material with high TD density separated by regions of much lower TD density. Figure 2(a) shows particularly clearly that there are alternating narrow and wide bands of TDs, with the overall periodicity (i.e., the distance from one narrow band to the next, perpendicular to the bands) being ~10 μm, corresponding to the period spacing of the ELOG mask.

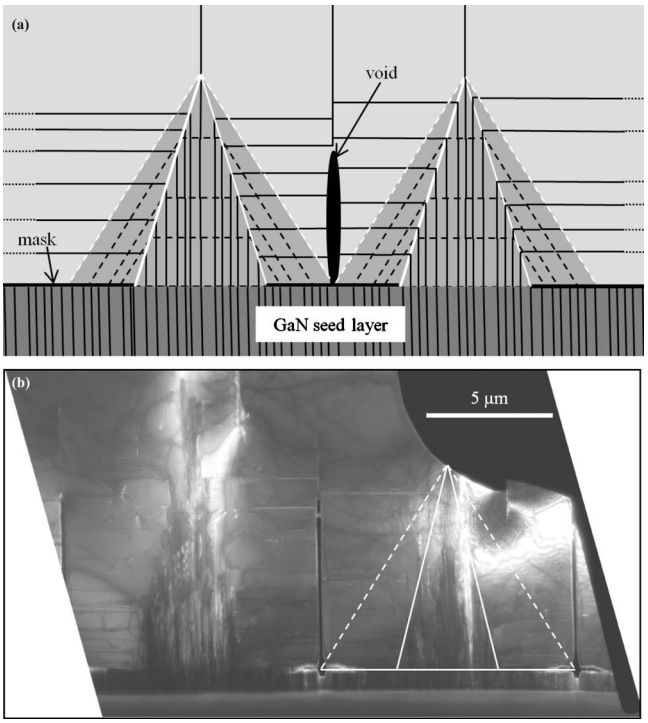

FIG. 3. (a) Schematic of the ELOG process. TDs are represented by solid black lines. (b) (0002) WBDF TEM image of the ELOG GaN sample. The white lines on the right-hand half of the image correspond to the white lines in (a) indicating the growth of the GaN stripe through the window region.

The alternating wide and narrow bands of TDs can be understood with reference to Fig. 3. Figure 3(a) shows a schematic of the two-step ELOG process. Dislocations propagate through the windows in the mask, but where they meet the $\{11\bar{2}2\}$ facets, they tend to bend over. Some dislocations propagate through the top of the triangular stripe and do not bend over. The dislocations which propagate laterally may be annihilated when the stripes coalesce since a void often forms at the coalescence boundary. Alternatively, interactions between dislocations may lead to dislocation annihilation or to the formation of dislocations at the coalescence boundary propagating in the growth direction. Hence, for each period of the mask pattern, we expect to see two bands of TD pits—one at the coalescence boundary, and one at the middle of the window region. The TEM data shown in Fig.

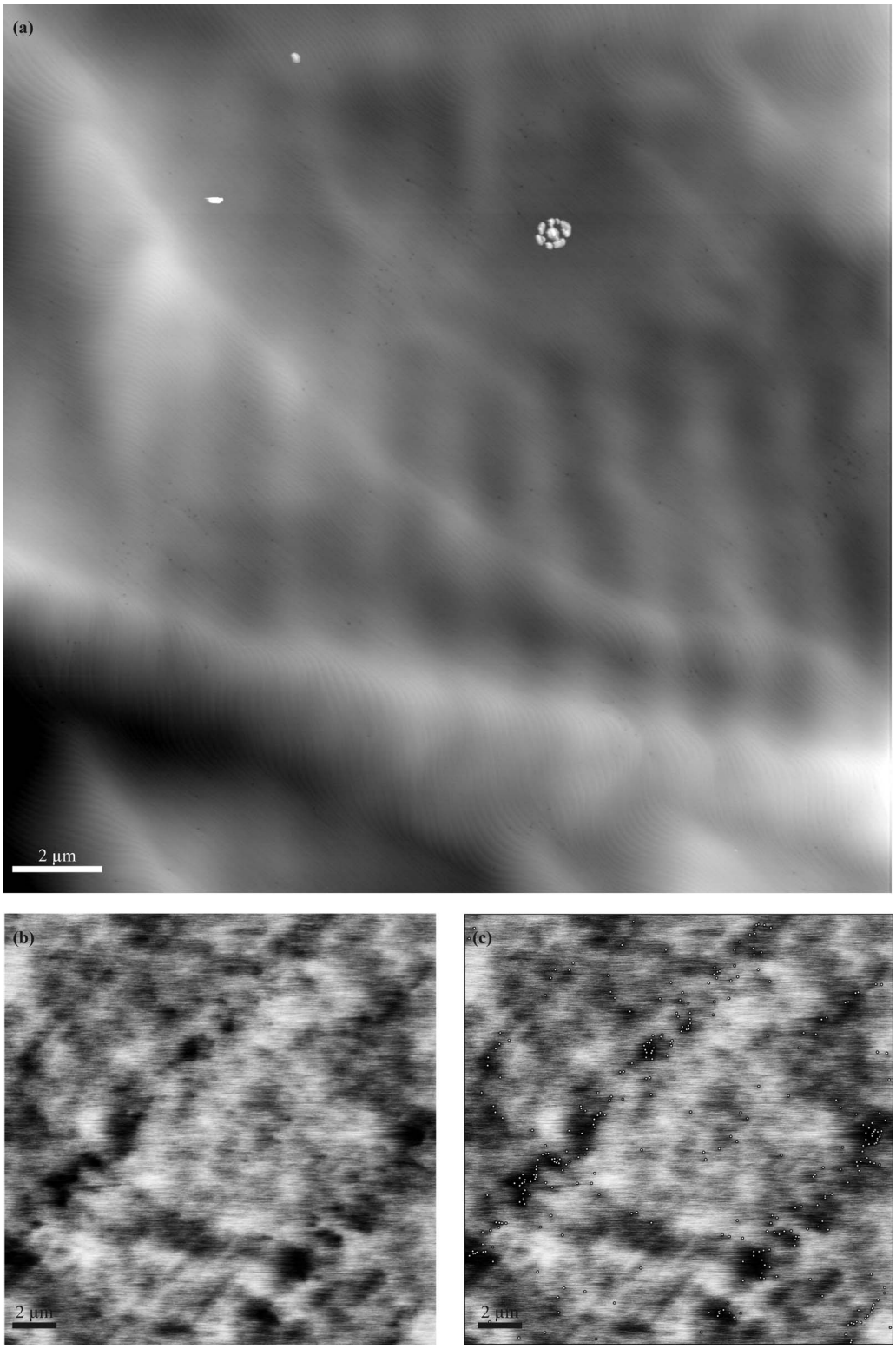

FIG. 4. (a) Topographic AFM image of ELOG GaN: 20×20 μm^2 image from a data set containing 2048×2048 pixels. $z=15$ nm. (b) KPFM data obtained simultaneously with (a). Voltage scale $(V)=107$ mV (c) KPFM image from (b) with black circles filled with white added to indicate the positions of the TD pits observed in (a). The detail from the original images in (a) and (b) may not be visible in print copies, so electronic versions of the original images are provided as online supplementary material (Ref. 18).

3(b) suggest that the narrow band of TDs seen in the AFM data in Figs. 1 and 2 relates to the coalescence boundary, whereas the broad band of TDs relates to defects propagating directly from the window in the mask. (The triangles shown in white on the schematic are also shown in white on one part of the TEM image, as a guide to the eye.) These data suggest that at the beginning of the lateral growth stage, (0001) facets still persisted at the top of the stripes of GaN, allowing dislocations to propagate in the growth direction. Hence, to improve the effectiveness of the ELOG process the

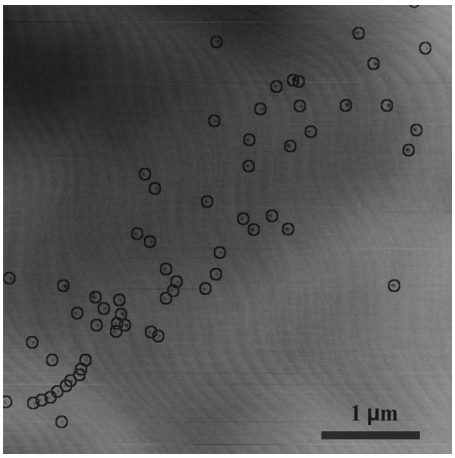

FIG. 5. A portion of the image shown in Fig. 1(a), which has been analyzed using PITS. The black rings show the positions of TD pits detected in the software.

initial growth stage should perhaps be extended. Broad area, high pixel-density AFM images could then be used to check the effectiveness of this strategy.

Figure 4(a) shows a 20×20 μm^2, 2048×2048 pixel AFM topography image, while Fig. 4(b) shows a corresponding surface potential (KPFM) image from the same area. (As with Fig. 1, electronic copies of the full high resolution images are also provided as supplementary online material.[18]) The KPFM data show bands of dark contrast running diagonally across the image. In Fig. 4(c), the positions of the TD pits observed in Fig. 4(a) are overlaid as black circles filled with white on the KPFM data in Fig. 4(b), showing that the clearest bands of dark contrast correspond to the broad bands of TDs seen in the topography image. Many but not all of the TDs seen between these broad bands also correspond to regions of locally lower potential. Also, some regions of dark contrast in the KPFM data do not seem to correlate with TD positions.

In previous studies of ELOG material using electrical scanning probe microscopy techniques (such as a recent conductive AFM study by Moore *et al.*[19]), specific features in electrical images were not linked to specific defects. Instead, the known periodicity of the ELOG sample was used to correlate regions of high defect density with local changes in electrical properties. The approach demonstrated here is more informative since it allows us to quantify the correspondence between actual defect sites and features in the electrical data set. A simple quantitative analysis will be described in Sec. IV.

IV. DATA ANALYSIS

In order to facilitate analysis of the large data sets shown above, a software tool called PITS has been developed for the automated detection of dislocations in JPEG images of AFM scans. The program comes with a user-friendly interface and is written in JAVA and thus is platform independent. Since it is applicable to JPEGs, a standard bitmap image format, it could be used to analyze AFM data from any microscope, not just the Veeco instrument used here. To request a free copy of the PITS software, readers should e-mail "pits@msm.cam.ac.uk."

TABLE I. Comparison of the dislocation densities found by manual counting and by the PITS program from three different 30×30 μm^2, 4992×4992 pixel images of ELOG GaN.

Image	Dislocation density measured manually (cm^{-2})	Dislocation density from PITS program (cm^{-2})
1	1.2×10^8	1.2×10^8
2	1.3×10^8	1.4×10^8
3	9.2×10^7	9.5×10^7

In PITS, several filters are applied to the image in order to enhance the contrast of the TD pits and to reduce the noise. The resulting image is then searched for sharp changes in surface gradient which are subsequently interpreted as TD pits. Several parameters of the filters can be changed to improve the quality of the pit detection. In the final stage, the pit selection can be modified by the user (i.e., wrongly detected pits can be removed and undetected pits can be added). The program allows export of the pits' coordinates in a text format for further analysis and statistical evaluation, such as the type of analysis performed by Moram *et al.*[20]

The most important part of the image processing is a calculation of absolute values of the x and y derivatives of the image. Depending on the image quality, the analysis can be performed from one of the derivatives or from their combination. Since the fast-scan direction of the AFM scan corresponds to the x direction, the scans often contain artificial contrast steps along the y direction (related to tip changes) and thus the analysis based on the x derivative gives better results. In the next step, the image (based on the absolute values of the derivatives) is blurred to reduce the noise. The blur filter replaces the intensity of a given pixel by the averaged intensity of that pixel and the four neighboring pixels. Subsequently, an intensity threshold filter is applied that cuts off the noise and leaves in the processed image only regions corresponding to sudden changes in the intensity (i.e., pits) in the original image. The threshold can be adjusted by the user in order to fine tune the pits' selection.

The output of the PITS program is illustrated in Fig. 5, which shows a section of the AFM topography image in Fig. 1(a) analyzed using the software. The black rings around the dislocations have been applied automatically in this case. For three 30×30 μm^2, 4992×4992 pixel AFM topography images of the ELOG sample, the dislocation density has been estimated both by manually counting all the TD pits and by using the PITS program. The results of the two approaches are shown in Table I, which illustrates the good agreement between the PITS results and the much more time-consuming manual approach.

For the topography image taken in parallel with KPFM data shown in Fig. 4, PITS has been used to extract a list of TD pit coordinates; there are more than 300 TD pits in the image. A separate routine using a MICROSOFT EXCEL MACRO has then been used to find the potential at each of the TD coordinates in the corresponding KPFM data set. The mean potential at the TD pit sites has been calculated and is 9.5

mV lower than the mean potential found for the image as a whole. A student t-test may be applied to test the hypothesis that the mean potential at the dislocation sites is lower than the mean potential across the entire image. The test suggests a confidence level significantly greater than 99.95% that the reduction in the mean potential at the dislocation sites is genuine. The high confidence level reflects the large number of data points used to calculate the mean values, illustrating the usefulness of collecting data on dislocations in GaN across large areas.

V. SUMMARY

We have demonstrated that using an AFM system with a high sampling rate, it is possible to image pits relating to TDs in GaN across large areas, even when in some cases the dislocations are closely spaced. This allows detailed examination of the spatial distribution of dislocations arising from techniques such as ELOG and may also be useful in imaging samples with particularly low dislocation densities. The analysis of the resulting AFM data may be automated and we have described a relevant software tool—PITS—which facilitates this process. In addition to broad area high pixel density topographic images, we have also recorded surface potential data simultaneously and have established a correlation between the presence of TD pits and a reduced local potential. However, detailed examination of the relevant data sets shows that not all TDs are associated with a reduction in surface potential. The pixel densities used in our images allow these types of details to be examined, which might not be picked up in lower resolution scans.

ACKNOWLEDGMENTS

This work has been funded, in part, by the EPSRC (Grant No. GR/S 49391/01). R.A.O. would like to acknowledge funding from the Royal Society.

[1] M. S. Ferdous, X. Wang, M. N. Fairchild, and S. D. Hersee, Appl. Phys. Lett. **91**, 231107 (2007).
[2] S. Nakamura, Science **281**, 956 (1998).
[3] S. Kamiyama, M. Iwaya, S. Takanami, S. Terao, A. Miyazaki, H. Amano, and I. Akasaki, Phys. Status Solidi A **192**, 296 (2002).
[4] Z. Bougrioua, M. Azize, P. Lorenzini, M. Laügt, and H. Haas, Phys. Status Solidi A **202**, 536 (2004).
[5] R. Datta, M. J. Kappers, J. S. Barnard, and C. J. Humphreys, Appl. Phys. Lett. **85**, 3411 (2004).
[6] C. Hemmingsson, M. Boota, R. O. Rahmatalla, M. Junaid, G. Pozina, J. Birch, and B. Monemar, J. Cryst. Growth **311**, 292 (2009).
[7] R. I. Barabash, C. Roder, G. E. Ice, S. Einfeldt, J. D. Budai, O. M. Barabash, S. Figge, and D. Hommel, J. Appl. Phys. **100**, 053103 (2006).
[8] J. L. Weyher, P. D. Brown, J. L. Rouviere, T. Wosinski, A. R. A. Zauner, and I. Grzegory, J. Cryst. Growth **210**, 151 (2000).
[9] C. Youtsey, L. T. Romano, R. J. Molnar, and I. Adesida, Appl. Phys. Lett. **74**, 3537 (1999).
[10] N. Kuwano, R. Tajima, S. Bohyama, H. Miyake, K. Hiramatsu, and T. Shibata, Phys. Status Solidi A **201**, 2755 (2004).
[11] H. W. Choi, C. Liu, M. G. Cheong, J. Zhang, and S. J. Chua, Appl. Phys. A: Mater. Sci. Process. **80**, 405 (2005).
[12] R. A. Oliver, M. J. Kappers, J. Sumner, R. Datta, and C. J. Humphreys, J. Cryst. Growth **289**, 506 (2006).
[13] M. A. Moram, M. J. Kappers, Z. H. Barber, and C. J. Humphreys, J. Cryst. Growth **298**, 268 (2007).
[14] R. A. Oliver, M. J. Kappers, C. McAleese, R. Datta, J. Sumner, and C. J. Humphreys, J. Mater. Sci.: Mater. Electron. **19**, 208 (2008).
[15] M. A. Moram, C. F. Johnston, M. J. Kappers, and C. J. Humphreys, J. Phys. D **43**, 055303 (2010).
[16] P. Gibart, Rep. Prog. Phys. **67**, 667 (2004).
[17] R. A. Oliver, Rep. Prog. Phys. **71**, 076501 (2008).
[18] See supplementary material at http://dx.doi.org/10.1063/1.3430539 for the full high resolution images for data in Figs. 1(a), 4(a), and 4(b).
[19] J. C. Moore, V. Kasliwal, A. A. Baski, X. Ni, U. Ozgur, and H. Morkoc, Appl. Phys. Lett. **90**, 011913 (2007).
[20] M. A. Moram, R. A. Oliver, M. Kappers, and C. J. Humphreys, Adv. Mater. **21**, 3941 (2009).